Scripta Materialia 208 (2022) 114325

Contents lists available at ScienceDirect

Scripta Materialia

journal homepage: www.elsevier.com/locate/scriptamat

Viewpoint set

Numerical investigation of the transient interfacial material behavior during laser impact welding

Glenn Gleason[a], Sumair Sunny[a], Ritin Mathews[a], Arif Malik[a,*]

Department of Mechanical Engineering, The University of Texas at Dallas, 800 W. Campbell Rd., Richardson, TX 75080, USA

ARTICLE INFO

Article history:
Received 22 June 2021
Revised 12 August 2021
Accepted 2 October 2021
Available online 17 October 2021

Keywords:
Laser impact welding
Eulerian model
Inhomogeneous microstructure
Thermal response
Plastic strain

ABSTRACT

During laser impact welding, severe plastic strains and temperature spikes occurring in less than 1 μs make experimental observation impractical and necessitate computational modeling to characterize in-situ behavior. To understand the effects of microstructure and the associated inhomogeneity/anisotropy in laser impact welding, an Eulerian framework featuring aluminum 1100 flyer and stainless steel 304 target foils is applied to simulate cases with and without microstructure modeling. The transient thermo-mechanical phenomena revealed by the dynamic simulation provide insights into evolution of the in-situ structure-property relationship, including microstructural variation, phase transformation, and material jetting. In contrast to the homogeneous model, the inhomogeneous model suggests a 10 μm-thick zone of grain refinement at the weld interface establishing new grains 0.1-1 μm in diameter in the flyer, and causing partial martensitic phase transformation in the target, attributable to rapidly induced equivalent plastic strains of up to 10.71 in the flyer and 0.98 in the target.

Solid state welding refers to a broad category of welding processes in which joints are created between materials without exceeding their respective melting points, or doing so only at small scales [1], thus permitting the joining of metals with dissimilar melting temperatures or other characteristics that render them unsuitable for fusion welding [2]. Within the solid-state category, impact welding is characterized by a bond achieved via high-speed collision, with a relative angle between the two surfaces to be joined [3]. An essential feature of impact welding is the jetting of particles from the weld front caused by ablative shearing, enabling direct contact between the parent materials without surface asperities or contaminants interfering with bonding during weld formation [4,5].

When the surfaces collide at an appropriate oblique angle and velocity to form a joint, extreme shear forces concentrate near the weld front and travel at velocities approaching the speed of sound in the materials [6]. Extreme localized plastic deformation also occurs, with concurrent elevated temperatures from plastic heat dissipation near the interface. The rapidly shearing surface material acts as an inviscid fluid [7] and ablates from the advancing weld front via a high velocity, high temperature jet [8]. The presence of a jet is thus considered a necessary condition of impact weld formation; however, at excessively high impact energy, melt pockets may form via vortex shedding [9], resulting in the formation of brittle intermetallics or other defects that reduce the efficiency of the joint.

While there are ongoing efforts aimed at observing impact weld processes in-situ [10,11], detailed observations into the transient evolution of strain and temperature fields remain impractical to obtain experimentally considering the short timeframe of the process (μ∼ 1s). Hence, the value of suitable analytical and computational models to address the experimental deficit is evident. Such models may offer insights into evolving conditions at the impact interface during weld formation, helping explain post-weld experimental observations. For instance, the formation of new high-angle grain boundaries via dynamic recrystallization has been experimentally observed in aluminum during severe plastic deformation processes [12–14]; an analogous computational model can allow better understanding of how comparable quantities of plastic deformation at laser impact welding (LIW) interfaces may result in increased grain boundary density, and thus increased hardness. Diffusion effects at impact weld interfaces are also of interest; at high energy levels in large-scale impact welds, the formation of defects such as brittle intermetallic zones [3] can pose concerns depending on the alloys welded. A computational model capable of predicting the transient thermomechanical effects at a newly formed interface can be useful for determining the likelihood of significant diffusion and subsequent chemical bonding effects.

The demonstrated numerical framework for LIW predicts thermomechanical responses such as plastic strain and corresponding

* Corresponding author.
E-mail address: Arif.Malik@utdallas.edu (A. Malik).

https://doi.org/10.1016/j.scriptamat.2021.114325
1359-6462/

heat dissipation using an Eulerian formulation, factoring in predicted microstructures for the two foils being joined. Such a computational framework is useful for impact welding problems due to extreme material deformation and mixing [15–21]. The Eulerian method utilizes a spatially fixed mesh that is fully remapped with each time increment, avoiding problems of mesh distortion that occur in Lagrangian [22] and Arbitrary Lagrangian-Eulerian formulations [23]. Eqs. (1) to (3) describe conservation of mass, momentum, and energy in the model, respectively.

$$\frac{\partial \rho}{\partial t} + \nabla \cdot (\rho \dot{\boldsymbol{X}}) = 0 \tag{1}$$

$$\frac{\partial \rho \dot{\boldsymbol{X}}}{\partial t} + \nabla \cdot \left(\rho \dot{\boldsymbol{X}} \otimes \dot{\boldsymbol{X}}\right) = \nabla \cdot \boldsymbol{\sigma} \tag{2}$$

$$\frac{\partial e}{\partial t} + \nabla \cdot \left(e \dot{\boldsymbol{X}}\right) = \boldsymbol{\sigma} : \dot{\boldsymbol{\varepsilon}}_{\boldsymbol{p}} \tag{3}$$

In Eqs. (1) to (3), ρ is the mass density, $\dot{\boldsymbol{X}}$ is the velocity vector, $\boldsymbol{\sigma}$ is the stress tensor, $\dot{\boldsymbol{\varepsilon}}_{\boldsymbol{p}}$ is the plastic strain rate tensor, t is time, and e is the internal energy per unit volume. These equations govern the Eulerian step, which calculates material transport within the Eulerian grid. Eqs. (1) to (3) can be generalized as:

$$\frac{\partial \boldsymbol{\phi}}{\partial t} + \nabla \cdot \boldsymbol{\Psi}(\boldsymbol{\phi}, \dot{\boldsymbol{X}}, \boldsymbol{X}, t) = \boldsymbol{S} \tag{4}$$

where $\boldsymbol{\Psi}$ is a flux function, $\boldsymbol{S}$ is a source function, $\boldsymbol{X}$ is the position vector, and $\boldsymbol{\phi}$ is a solution variable. Operator splitting in (4) gives (5) and (6), which are solved in separate steps during each time increment.

$$\frac{\partial \boldsymbol{\phi}}{\partial t} = \boldsymbol{S} \tag{5}$$

$$\frac{\partial \boldsymbol{\phi}}{\partial t} + \nabla \cdot \boldsymbol{\Psi}(\boldsymbol{\phi}, \dot{\boldsymbol{X}}, \boldsymbol{X}, t) = \boldsymbol{0} \tag{6}$$

(5) resembles the Lagrangian governing equation, except for the substitution of the spatial time derivative for the material time derivative on the left side. Solution variables are calculated on a temporary Lagrangian mesh within a sufficiently small time increment to avoid displacement across more than one element length. After mesh remapping, (6) is solved to account for changes in solution variables on the fixed mesh due to advection. In this manner, quantities such as equivalent plastic strain, internal energy, and mass can be tracked throughout the impact weld process [24].

Two cases of the LIW simulation described here are established, differing only in constitutive and microstructural material models for the flyer and target foil pairs. The first is a homogeneous material model, using the assumption of a single quasi-static yield strength in the Johnson-Cook flow stress model for the aluminum 1100 flyer with an H19 heat treatment and an annealed stainless steel (SS 304) target. The second is an inhomogeneous model, with the foils' microstructures predicted via a Dynamic Kinetic Monte Carlo (KMC) model [25,26]. This Dynamic KMC model is adapted from the open source KMC model published by Sandia in 2017 [27] by adding modifications that capture effects of transient intralayer and interlayer heat accumulation on the predicted microstructure. Here, variable reference yield strengths among metallic grains in the foils are established according to a combined Johnson-Cook Hall-Petch (J-C H-P) constitutive model for both materials. Hydrostatic elastic behavior is governed by a Mie-Grüneisen equation of state, and a linear shear stress-strain relation is also applied. In both models, the inelastic heat fraction is set to 0.9 [28]; this estimate is consistent with the plastic heat dissipation behavior of both aluminum 1100 [29] and SS 304 [30] at the high strains (>20%) that are characteristic of impact weld interfaces. A comprehensive description of the computational model can be referenced from an earlier publication by the authors [26], and the overall LIW modeling approach without microstructure has shown good agreement with the weld geometry resulting from experiment [18]. However, findings presented here reveal novel insights toward how the transient impact welding phenomena influence microstructural variation and phase transformation.

The finite element model representing the LIW process is depicted in Fig. 1. An Eulerian grid defines the control volume for the entire system, with active material volume fractions imposed at the locations of the 50 μm-thick flyer and target foils. The elements are linear hexahedral, with fully coupled mechanical and thermal solutions. A standoff of 260 μm initially separates the flyer and target, consistent with successful joints formed in experiments [18,31]. Since Raoelison et al. [32] observed that impact weld joints were formed without interfacial slip or separation, the no-slip contact condition imposed between Eulerian materials reflects conditions of extreme contact pressure relative to lateral forces at the weld interface.

Simplifications to the model have been introduced to reduce computational expense; a plane strain assumption is applied based on observations by Lee et al. indicating substantial consistency in impact weld morphology in the direction normal to the weld cross-section over large distances relative to the flyer thickness [33]. Additionally, a void is placed within the Eulerian grid in the volume not occupied by the foils. Both the confining overlay atop the flyer and substrate underneath the target are represented by rigid bodies under fixed-displacement boundary conditions. The domain of investigation is limited to the path of contact between the foils as the collision progresses from the center (X = 0) outward, and thus the foil lengths are limited to 600 μm. Solutions are computed using the explicit solver of Abaqus v6.14.

To model realistic deformation and internal stress response during its approach to the target, the flyer is loaded with a Gaussian plasma pressure spatial profile as seen in Fig. 1. This pressure varies in time according to a 1D hydrodynamic model [34] used to represent the transient behavior of the expanding, confined plasma induced by a nanosecond-pulsed near-infrared laser having a circular area of irradiance with 1.6 mm radius. A 2.7 GPa peak pressure is achieved after 17 ns, at the end of the active laser pulse.

The state of the collision at $t = 425$ ns is illustrated in Fig. 2, and suggests no apparent weld formation in either case, due to the lack of jetting predicted at the interface. The relatively small local collision angle inhibits initiation of the shear instability necessary to ablate the flyer and target surfaces under high pressure and bring the alloys into interatomic-scale contact. However, the collision causes a localized increase in temperature due to volumetric compression, an effect modeled by the equation of state, which in turn causes a decrease in flow stresses at the leading edge where the foils make contact. This results in subsequent weld initiation at $t = 450$ ns, as the collision point progresses to 0.2 mm in the X direction. Near the laser spot center ($0 \leq X < 0.2$ mm), reflected pressure waves may cause internal spallation and rebound, as has been observed in experiments by Wang et al. [31,35]. A transient temperature-rise caused by compressive stress near the rigid substrate is predicted in the region below the laser spot center (corresponding to the bottom left) in the target in both cases, Fig. 2 (*Top center, Top right*). Subtle differences between the inhomogeneous and homogeneous models are predicted at this stage; peak equivalent plastic strains reach 0.976 within the aluminum flyer in the inhomogeneous model, versus 0.829 in the homogeneous model, and the highest temperatures are 1425 and 1370 K, respectively.

As the imposed pressure load on the flyer foil reaches a maximum at the central laser beam axis, the resulting Y-component of the velocity, v_Y, is also at a maximum magnitude at the same

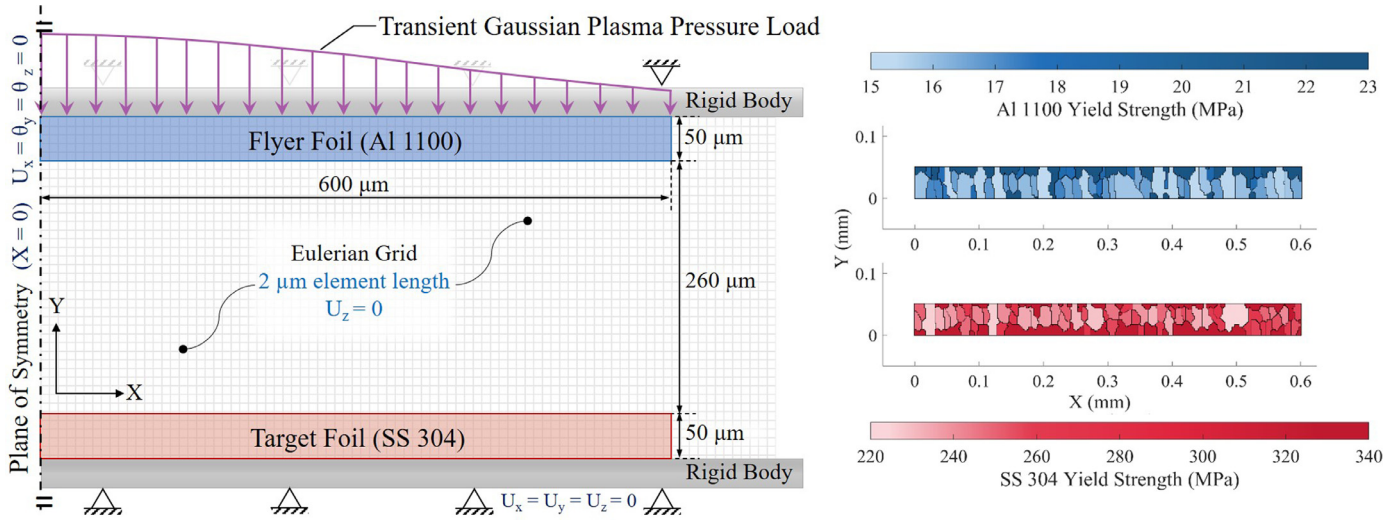

Fig. 1. Graphical overview of the LIW process model, adapted from [26]: (*Left*) Geometry of the active material volume fractions in the Eulerian grid, rigid body placements, and boundary conditions. (*Right*) Microstructural configuration of the foils, with legends indicating yield strengths of respective grains. This figure has been adapted with permission from [26]. (For interpretation of the reference to color in the figure, the reader is referred to the online version of this article.)

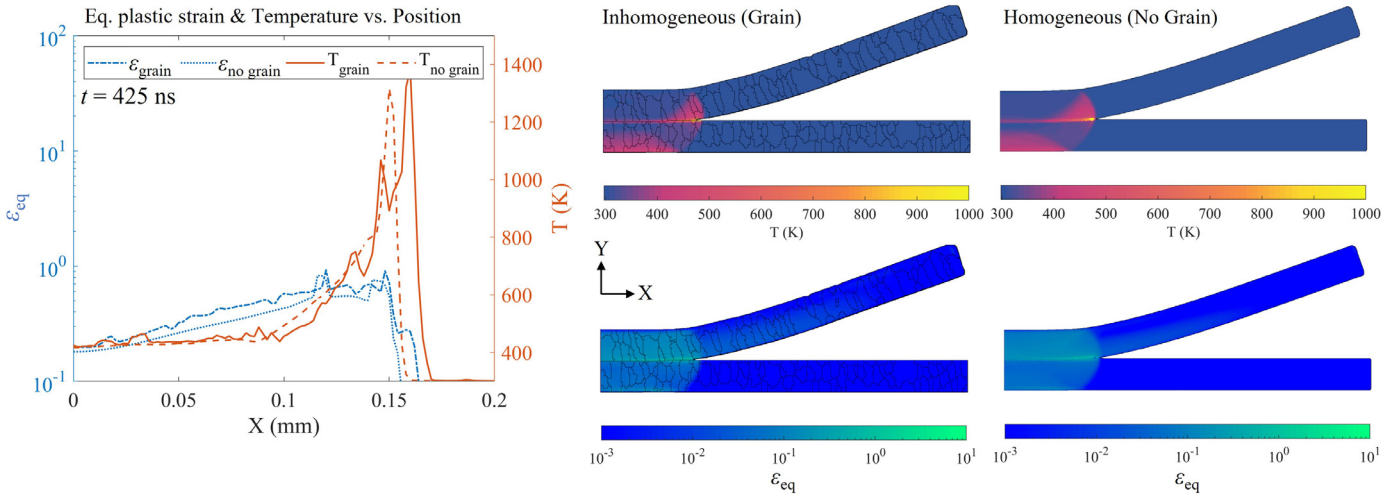

Fig. 2. Material response immediately post-impact, at $t = 425$ ns. (*Left*) Comparison of the localized temperature (T) and equivalent plastic strain (ε_{eq}) sampled along the contact interface in both inhomogeneous (grain) and homogeneous (no grain) models. (*Top center*) Temperature distribution for grained model, and (*Top right*) homogeneous model; (*Bottom center*) Equivalent plastic strain distribution for grained model, and (*Bottom right*) homogeneous model. (For interpretation of the reference to color in the figure, the reader is referred to the online version of this article.)

point, and the flyer approaches the target at 683.4 m s^{-1} after 400 ns. In both the homogeneous and inhomogeneous cases, the LIW simulation predicts contact between the flyer and target at $t = 400$ ns, and a collision point forms that rapidly advances in the +X direction during the weld period of $400 \leq t \leq 800$ ns. A declining v_Y profile along the flyer in the +X direction results in the flyer maintaining a curved shape ahead of the collision point throughout the weld phase. Fig. 3 (*Left*) illustrates the decline of the collision velocity, v_X, after 450 ns as energy is dissipated via mutual ablation of the colliding surfaces, with the associated plastic heat dissipation.

The collision point accelerates briefly in the +X direction, until a prerequisite v_X is reached at 450 ns to form the jet, and thus initiate the weld. Such extreme flow velocities of the jet, containing material from both the flyer and target, cause instabilities that can result in the formation of a wavy interface [36]. Peak v_X in the inhomogeneous case reaches 3850 m s^{-1} at $t = 450$ ns, slightly lower than the 4050 m s^{-1} in the homogeneous case; however, collision velocity declines more slowly in the inhomogeneous case than the homogeneous case beyond $t = 525$ ns. The presence of very small grains on the surface of the SS 304 foil, having a greater flow stress as per the J-C H-P material model, suggests reduced plastic heat dissipation during weld progression across the target surface.

At $t = 500$ ns (Fig. 4), a weld is underway with both cases now exhibiting jetting, and the pronounced thermal and plastic strain fronts seen earlier in Fig. 2 have become less distinct. An important consideration in the development of the inhomogeneous material model is the accuracy of the predicted microstructure under extreme thermal and plastic strain conditions, as the framework does not reveal effects of dynamic recrystallization. Regions where the equivalent plastic strain exceeds 1 in the aluminum flyer, predicted in a narrow band of approximately 10 μm thickness near the weld interface, from $0.15 < X < 0.4$ mm, suggest the propensity for grain refinement [37]. A peak equivalent plastic strain of 10.71 is reached at the interface, well beyond the refinement threshold; the plastic strains predicted along the growing weld are similar to those caused via processes of severe plastic deformation, with

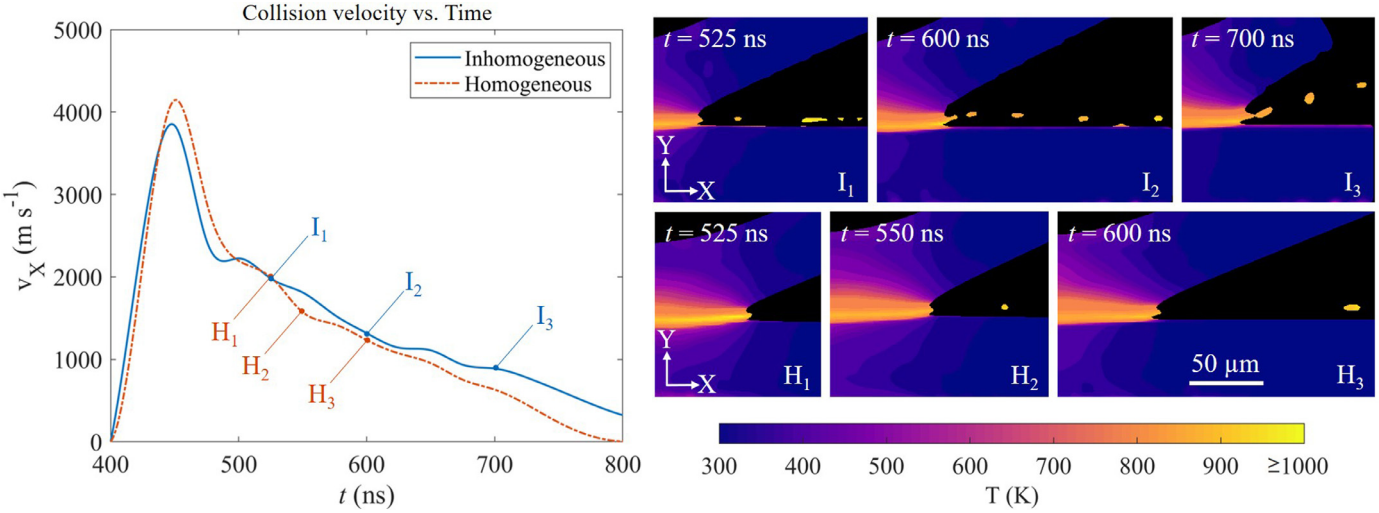

Fig. 3. (*Left*) Comparison of collision velocity, v_X, for the inhomogeneous (grain) and homogeneous (no grain) cases. (*Right*) Key frames from the inhomogeneous (I) and homogeneous (H) simulations, illustrating differences in jetted material volume and local temperatures. Grain boundaries are omitted in the inhomogeneous frames (I) for clarity. This figure has been reprinted with permission from [26]. (For interpretation of the reference to color in the figure, the reader is referred to the online version of this article.)

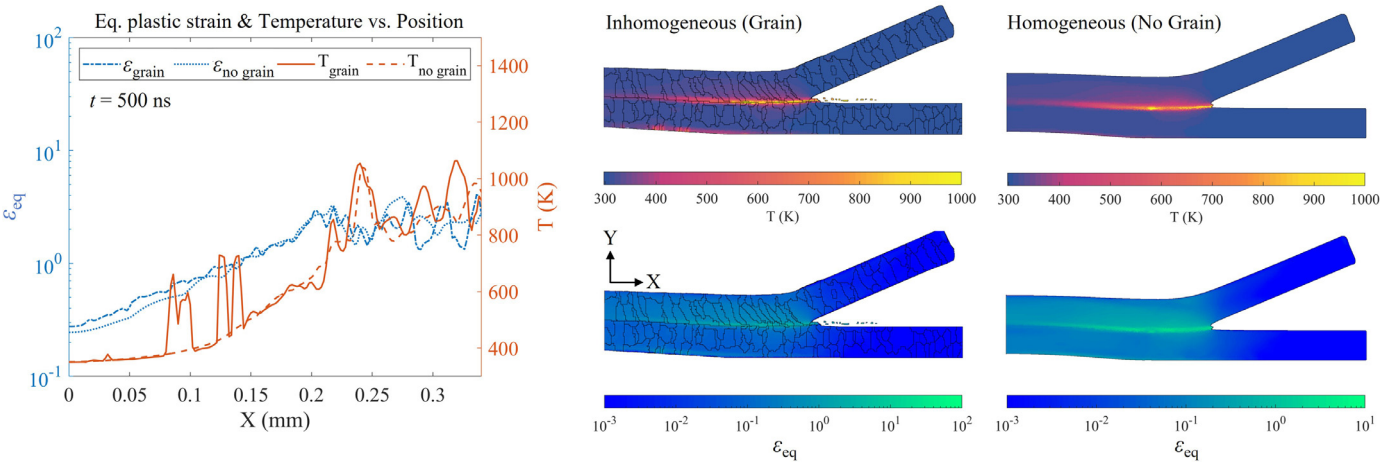

Fig. 4. Material response at t = 500 ns. (*Left*) Comparison of the localized temperature (T) and equivalent plastic strain (ε_{eq}) sampled along the contact interface in both inhomogeneous (grain) and homogeneous (no grain) models. (*Top center*) Temperature distribution for grained model, and (*Top right*) homogeneous model; (*Bottom center*) Equivalent plastic strain distribution for grained model, and (*Bottom right*) homogeneous model. (For interpretation of the reference to color in the figure, the reader is referred to the online version of this article.)

grain sizes ranging from 0.1 to 1 µm likely arising in the aluminum flyer [12,13]. This level of grain refinement within the flyer material in the weld zone also suggests an increase in the alloy's hardness [14].

In both LIW models, reflected elastic stress waves and shear instabilities at the weld front cause slight fluctuations in equivalent plastic strains along the interface. These effects are revealed by constitutive modeling that allows periodic instability to emerge in the plastic strain predicted along the weld interface, a phenomenon observed in experimental impact welding literature [15,16]. Previous studies have investigated the role of unstable motion during the advancement of the collision point as a prerequisite for the jet that indicates the formation of welds [36,38,39]. Due to the variation of flow stresses along the interface, the inhomogeneous model predicts a more pronounced jet, suggesting greater instabilities that initiate among the metallic grains as the collision point advances [26]; the homogeneous case, by contrast, has no microstructural variation and predicts far less jetted material. The reader is referred to the supplementary material for LIW animations illuminating the new, in-situ transient phenomena.

Fig. 5 presents the material response at t = 600 ns, with the inhomogeneous case showing less prominent concentrations of elevated temperature and plastic strains than the earlier frames, with the notable exception of a thermal spike of 1475 K at X = 0.35 mm. This extreme temperature corresponds to a high shock pressure at a small grain of SS 304; the applied equation of state accounts for a large, localized increase in temperature but does not capture phase change, thus likely reflecting only localized melting that persists for a brief duration. Recent experimental work by Bellmann et al. [11,40] analyzed light spectra from forming impact welds that indicated temperatures above vaporization thresholds for copper and aluminum, suggesting the plausibility of localized temperature spikes due to transient shock and plastic dissipation effects, particularly when a grained microstructure is considered. While the welding process has not yet completed, the maximum plastic strain values for both LIW simulations are reached at the interface. These plastic strain values suggest that exothermic martensitic phase transformation can be expected in the SS 304 target, an effect that drives the inelastic heat fraction to over 1 at equivalent plastic strains ranging from 0.07 up to 0.25 [30]; however, the

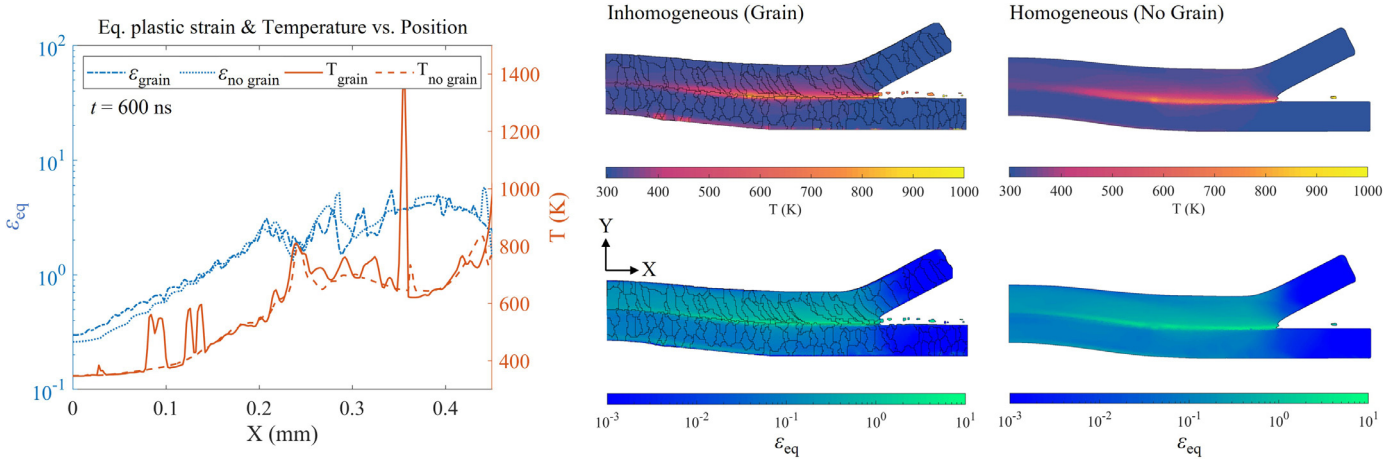

Fig. 5. Material response at t = 600 ns. (*Left*) Comparison of the localized temperature (T) and equivalent plastic strain (ε_{eq}) sampled along the contact interface in both inhomogeneous (grain) and homogeneous (no grain) models. (*Top center*) Temperature distribution for grained model, and (*Top right*) homogeneous model; (*Bottom center*) Equivalent plastic strain distribution for grained model, and (*Bottom right*) homogeneous model. (For interpretation of the reference to color in the figure, the reader is referred to the online version of this article.)

transformation will be limited due to the extreme strain rates observed in the model ($10^6 < \dot{\varepsilon}_p < 10^7$) near the weld. This renders a constant inelastic heat fraction of 0.9 a reasonable estimate, considering the high interfacial plastic strain values. Equivalent plastic strains within the target range up to 0.98 at the weld; on that basis, the martensitic transformation will likely be limited to under 20% in a narrow region, concentrated at shear bands which function as nucleation sites [41].

Findings from this study illuminate the potential of an Eulerian numerical model to capture the small-scale dynamic material responses of LIW, as it can readily accommodate material tracking under extreme deformation. While transient thermal and plastic strain responses during the impact welding process remain experimentally infeasible to observe directly, the demonstrated framework offers a suitable avenue for researchers to investigate how these transient phenomena influence microstructural variations and phase transformations along the interface.

Declaration of Competing Interest

The authors declare that they have no known competing financial interests or personal relationships that could have appeared to influence the work reported in this paper.

Supplementary material

Supplementary material associated with this article can be found, in the online version, at doi:10.1016/j.scriptamat.2021.114325.

References

[1] J. Guo, Solid state welding processes in manufacturing, Handbook of manufacturing engineering and technology (2015) 569–592.
[2] B. Crossland, A. Bahrani, Fundamentals of explosive welding, Contemp Phys 9 (1) (1968) 71–87.
[3] W. Cai, G. Daehn, A. Vivek, J. Li, H. Khan, R.S. Mishra, M. Komarasamy, A state-of-the-art review on solid-state metal joining, J. Manuf. Sci. Eng. 141 (3) (2019) 031012.
[4] G.R. Cowan, A.H. Holtzman, Flow configurations in colliding plates: explosive bonding, J Appl Phys 34 (4) (1963) 928–939.
[5] A. Deribas, I. Zakharenko, Surface effects with oblique collisions between metallic plates, Combustion, Explosion and Shock Waves 10 (3) (1974) 358–367.
[6] P. Groche, M. Becker, C. Pabst, Process window acquisition for impact welding processes, Materials & Design 118 (2017) 286–293.
[7] J. Robinson, Fluid mechanics of copper: viscous energy dissipation in impact welding, J Appl Phys 48 (6) (1977) 2202–2207.
[8] J. Pearson, Metal working with explosives, JOM 12 (9) (1960) 673–681.
[9] J. Robinson, The mechanics of wave formation in impact welding, The Philosophical Magazine: A Journal of Theoretical Experimental and Applied Physics 31 (3) (1975) 587–597.
[10] P. Groche, B. Niessen, C. Pabst, Process boundaries of collision welding at low energies, Materwiss Werksttech 50 (8) (2019) 940–948.
[11] J. Bellmann, J. Lueg-Althoff, B. Niessen, M. Böhme, E. Schumacher, E. Beyer, C. Leyens, A.E. Tekkaya, P. Groche, M.F.-X. Wagner, et al., Particle ejection by jetting and related effects in impact welding processes, Metals (Basel) 10 (8) (2020) 1108.
[12] Z. Horita, T. Fujinami, M. Nemoto, T.G. Langdon, Equal-channel angular pressing of commercial aluminum alloys: grain refinement, thermal stability and tensile properties, Metallurgical and Materials Transactions A 31 (3) (2000) 691–701.
[13] H. Adachi, Y. Miyajima, M. Sato, N. Tsuji, Evaluation of dislocation density for 1100 aluminum with different grain size during tensile deformation by using in-situ x-ray diffraction technique, Materials Transactions (2015) L–M2015803.
[14] Y. Ito, K. Edalati, Z. Horita, High-pressure torsion of aluminum with ultrahigh purity (99.9999%) and occurrence of inverse hall-petch relationship, Materials Science and Engineering: A 679 (2017) 428–434.
[15] R.N. Raoelison, T. Sapanathan, E. Padayodi, N. Buiron, M. Rachik, Interfacial kinematics and governing mechanisms under the influence of high strain rate impact conditions: numerical computations of experimental observations, J Mech Phys Solids 96 (2016) 147–161.
[16] T. Sapanathan, R.N. Raoelison, E. Padayodi, N. Buiron, M. Rachik, Depiction of interfacial characteristic changes during impact welding using computational methods: comparison between arbitrary lagrangian-eulerian and eulerian simulations, Materials & Design 102 (2016) 303–312.
[17] V. Gupta, T. Lee, A. Vivek, K.S. Choi, Y. Mao, X. Sun, G. Daehn, A robust process-structure model for predicting the joint interface structure in impact welding, J. Mater. Process. Technol. 264 (2019) 107–118.
[18] S. Sadeh, G.H. Gleason, M.I. Hatamleh, S.F. Sunny, H. Yu, A.S. Malik, D. Qian, Simulation and experimental comparison of laser impact welding with a plasma pressure model, Metals (Basel) 9 (11) (2019) 1196.
[19] S.A. Mousavi, S. Al-Hassani, Numerical and experimental studies of the mechanism of the wavy interface formations in explosive impact welding, J Mech Phys Solids 53 (11) (2005) 2501–2528.
[20] G. Gleason, S. Sunny, S. Sadeh, H. Yu, A. Malik, Eulerian modeling of plasma-pressure driven laser impact weld processes, Procedia Manuf. 48 (2020) 204–214.
[21] T. Lee, A. Nassiri, T. Dittrich, A. Vivek, G. Daehn, Microstructure development in impact welding of a model system, Scr Mater 178 (2020) 203–206.
[22] A. Nassiri, G. Chini, A. Vivek, G. Daehn, B. Kinsey, Arbitrary lagrangian–eulerian finite element simulation and experimental investigation of wavy interfacial morphology during high velocity impact welding, Materials & Design 88 (2015) 345–358.
[23] A. Nassiri, S. Zhang, T. Lee, T. Abke, A. Vivek, B. Kinsey, G. Daehn, Numerical investigation of CP-Ti & cu110 impact welding using smoothed particle hydrodynamics and arbitrary lagrangian-eulerian methods, J Manuf Process 28 (2017) 558–564.
[24] D.J. Benson, A mixture theory for contact in multi-material eulerian formulations, Comput Methods Appl Mech Eng 140 (1–2) (1997) 59–86.
[25] S. Sunny, H. Yu, R. Mathews, A. Malik, W. Li, Improved grain structure prediction in metal additive manufacturing using a dynamic kinetic monte carlo framework, Addit. Manuf. 37 (2021) 101649.
[26] S. Sunny, G. Gleason, R. Mathews, A. Malik, Simulation of laser impact welding for dissimilar additively manufactured foils considering influence of inhomogeneous microstructure, Materials & Design 198 (2021) 109372.

[27] T.M. Rodgers, J.D. Madison, V. Tikare, Simulation of metal additive manufacturing microstructures using kinetic monte carlo, Comput. Mater. Sci 135 (2017) 78–89.
[28] X. Wang, X. Wang, F. Li, J. Lu, H. Liu, Interface kinematics of laser impact welding of ni and SS304 based on jet indentation mechanism, Metallurgical and Materials Transactions A 51A (6) (2020) 2893–2904.
[29] D. Macdougall, Determination of the plastic work converted to heat using radiometry, Exp Mech 40 (3) (2000) 298–306.
[30] R. Zaera, J.A. Rodríguez-Martínez, D. Rittel, On the taylor–quinney coefficient in dynamically phase transforming materials. application to 304 stainless steel, Int. J. Plast. 40 (2013) 185–201.
[31] X. Wang, Y. Gu, T. Qiu, Y. Ma, D. Zhang, H. Liu, An experimental and numerical study of laser impact spot welding, Materials & Design (1980–2015) 65 (2015) 1143–1152.
[32] R.N. Raoelison, T. Sapanathan, N. Buiron, M. Rachik, Magnetic pulse welding of al/al and al/cu metal pairs: consequences of the dissimilar combination on the interfacial behavior during the welding process, J Manuf Process 20 (2015) 112–127.
[33] T. Lee, S. Zhang, A. Vivek, G. Daehn, B. Kinsey, Wave formation in impact welding: study of the cu–ti system, CIRP Ann. 68 (1) (2019) 261–264.
[34] R. Fabbro, J. Fournier, P. Ballard, D. Devaux, J. Virmont, Physical study of laser-produced plasma in confined geometry, J Appl Phys 68 (2) (1990) 775–784.
[35] X. Wang, F. Li, T. Huang, X. Wang, H. Liu, Experimental and numerical study on the laser shock welding of aluminum to stainless steel, Opt Lasers Eng 115 (2019) 74–85.
[36] A. Nassiri, B. Kinsey, G. Chini, Shear instability of plastically-deforming metals in high-velocity impact welding, J Mech Phys Solids 95 (2016) 351–373.
[37] H. Pirgazi, A. Akbarzadeh, R. Petrov, L. Kestens, Microstructure evolution and mechanical properties of aa1100 aluminum sheet processed by accumulative roll bonding, Materials Science and Engineering: A 497 (1–2) (2008) 132–138.
[38] X. Wang, T. Huang, Y. Luo, H. Liu, Laser indirect shock welding of fine wire to metal sheet, Materials (Basel) 10 (9) (2017) 1070.
[39] H. Wang, D. Liu, J.C. Lippold, G.S. Daehn, Laser impact welding for joining similar and dissimilar metal combinations with various target configurations, J. Mater. Process. Technol. 278 (2020) 116498.
[40] J. Bellmann, J. Lueg-Althoff, S. Schulze, S. Gies, E. Beyer, A.E. Tekkaya, in: Key Engineering Materials, 767, Trans Tech Publ, 2018, pp. 431–438.
[41] J.-Y. Choi, W. Jin, Strain induced martensite formation and its effect on strain hardening behavior in the cold drawn 304 austenitic stainless steels, Scr Mater 36 (1) (1997) 99–104.